



Cite this: *Nanoscale*, 2019, **11**, 19561

Heat generation by branched Au/Pd nanocrystals: influence of morphology and composition†

Marta Quintanilla, ^{a,b} Christian Kuttner, ^a Joshua D. Smith,^c Andreas Seifert, ^{d,e} Sara E. Skrabalak ^{*c} and Luis M. Liz-Marzán ^{*a,e}

Bimetallic gold–palladium particles were originally proposed as catalysts with tunable reaction rates. Following the development of synthesis routes that offer better control on the morphology and composition of the particles, novel optical sensing functionalities were more recently proposed. Since temperature is a fundamental parameter that interplays with every other proposed application, we studied the light-to-heat conversion ability of Au/Pd bimetallic nanoparticles with a regular octapodal shape. Both compositional (Au-to-Pd ratio) and structural (diagonal tip-to-tip distance and tip width) characteristics were screened and found to be essential control parameters to promote light absorption and efficient conversion into heat. Electromagnetic simulations reveal that the Pd content, and specifically its distribution inside the branched particle geometry, has a profound impact on the optical properties and is an essential criterion for efficient heating. Notably, the optical and photothermal responses are shown to remain stable throughout extended illumination, with no noticeable structural changes to the branched nanocrystals due to heat generation.

Received 5th July 2019,
Accepted 1st September 2019

DOI: 10.1039/c9nr05679c

rsc.li/nanoscale

Introduction

The microscopic characteristics of a material, such as lattice parameters or the presence of defects, are fundamentally connected to its physicochemical properties. In the case of palladium, when a thin layer is epitaxially grown on top of a different metal, the spacing of its first-neighbour atoms is modified, triggering changes in the position and overlap of the materials' d-orbitals and, thus, the electronic properties of the surface. Given that palladium is often used as a catalyst, this ability to change the electronic structure of surfaces opens up a path to create materials with tuned reaction rates, using either macroscale¹ or nanoscale structures.^{2–5} Nanocatalysts have gained particular attention as they open the possibility of triggering reactions in remote locations. This is the case, for instance, for tumour tissues, where they can be used to initiate pathological effects. Indeed, a range of techniques based on localized catalysis have been proposed as possible

intratumoral therapies, including chemodynamic therapy, gas therapy or tumour-starving therapy, to cite some.⁶

The interest on the synthesis of colloidal bimetallic structures is further supported by the added functionalities that nanometre sizes bring. Specifically, gold-rich nanocrystals may also present plasmonic resonances that can be exploited for optical applications, such as sensors based on refractive index modifications or on surface-enhanced Raman spectroscopy.^{7,8} Just as the catalytic activity of the colloids depends on their size and shape (*i.e.*, facet expression), the plasmonic properties of colloids are also linked to these parameters. In fact, their resonance wavelengths are closely linked to such structural parameters and can be tuned within the visible and the near-infrared range.⁹ Also, the character of the plasmonic mode, *i.e.*, to what extent it is due to scattering or absorption, depends on particle geometry and composition, and so do the possible functionalities of the resulting material. Particularly, while elastic scattering (Sca) can affect the density of phonon or photon states of surrounding molecules, eventually leading to the enhancement of their luminescent or Raman signals,^{10,11} absorption (Abs) is linked to the particles heating characteristics.^{12–14} As a consequence, synthetic routes that allow tuning the size and shape of bimetallic structures, LSPR position, and Abs/Sca ratio, gain relevance.¹⁵

Theoretical studies have demonstrated that in a nanoparticle only the fraction of material close to the surface efficiently contributes to heating, whereas the inner fraction hardly does. Accordingly, the most advantageous geometries

^aCIC biomAGUNE and CIBER-BBN, Paseo Miramón 182, 20014 Donostia-San Sebastián, Spain. E-mail: llizmarzan@cicbiomagune.es

^bMaterials Physics Department, Facultad de Ciencias, Universidad Autónoma de Madrid, 28049 Madrid, Spain

^cDepartment of Chemistry, Indiana University, Bloomington, Indiana, 47405, USA. E-mail: sskrabalak@indiana.edu

^dCIC nanoGUNE, Avda. Tolosa 76, 20018 Donostia-San Sebastián, Spain

^eIkerbasque, Basque Foundation of Science, 48013 Bilbao, Spain

† Electronic supplementary information (ESI) available: Details on synthesis, experimental methods, and simulations. See DOI: 10.1039/c9nr05679c



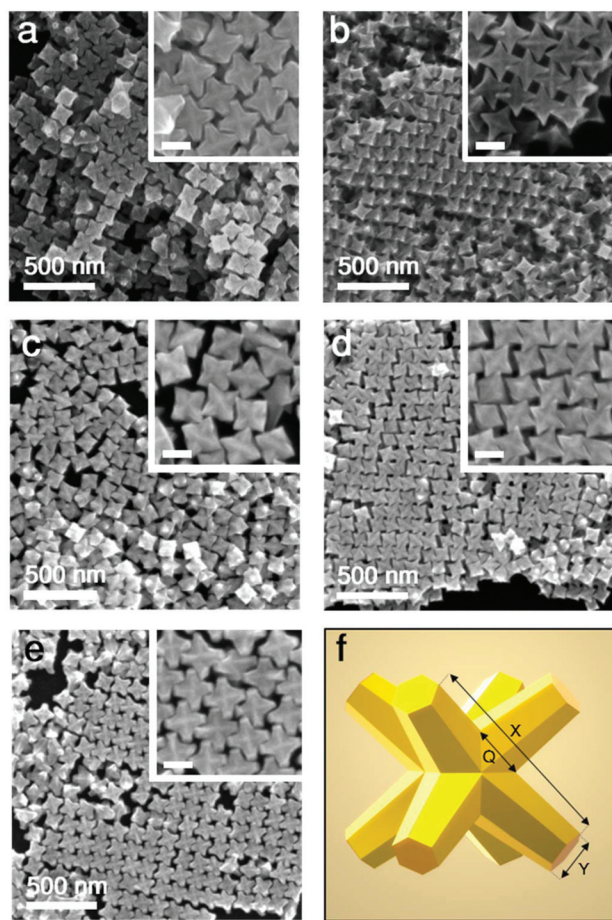


Fig. 1 Octopod morphologies: (a–e) SEM images of Au/Pd nanocrystals (samples A–E, labelled in order) of different dimensions and Au/Pd compositions (see Table 1). Scale bars in insets: 100 nm. (f) Schematic depiction of an octopod with indicated main structural parameters: face diagonal tip-to-tip length X , tip width Y , and branch base width Q .

(≈ 130 or ≈ 144 nm) and two tip widths (≈ 10 or ≈ 27 nm). A complete description of the tip morphology should also include the width of their base Q , which is roughly the same ($\approx 58 \pm 7$ nm) within the set of samples investigated. In addition, to understand the effect of the presence of Pd, we prepared samples with two different Pd contents ($\approx 8.7\%$ and $\approx 13\%$). For details, see Table 1. For further clarity, visual representations are provided in Fig. S2.†

Octopods can feature a variety of intense plasmon modes, depending on their morphology and composition, as shown in previous works.⁸ Accordingly, the main dipolar-like LSPR at low energy can be tuned throughout the visible and near-infrared ranges by varying these parameters. We chose to perform light-to-heat conversion experiments at a fixed wavelength of 808 nm, which falls within the near-infrared transparency region of water and minimizes heat transfer to the solvent. Besides, as it matches also a transparency window of haemoglobin,^{31,32} it is a technologically relevant wavelength for optical sensors that can be used in aqueous environments,



Fig. 2 Optical properties of octopods dispersed in water. Normalized UV/Vis/NIR extinction spectra showing intense plasmon bands close to the excitation wavelength (808 nm, grey dashed line).

as well as for biomedical applications including *in vivo* or *in vitro* catalysis,^{33,34} and photodynamic therapy.³⁵ Since the study requires octopods with the plasmon mode close to 808 nm, the range in which size and composition parameters can be varied is limited. To clarify this aspect, a discussion on the impact of the structural parameters X , Y , and Q on the LSPR position and intensity performed through FDTD simulations can be found in the ESI (section ESI.6†).

Fig. 2 shows the extinction spectra of the five samples under study, which were synthesized to overlap with the illumination wavelength as well as possible. The aim to unravel the relationship between composition, geometry and heating efficiency of the nanoparticles imposes restrictions on the number of variables that can be changed between samples. As a result, some particles (in particular sample B) present a certain mismatch between LSPR and laser wavelength. In the following sections we will consider this mismatch as an additional parameter for discussion.

At the plasmon resonance wavelength, the interaction of the particles with light is strong, and it can occur through either light scattering or light absorption. As mentioned above, the ability to transform light into heat is directly linked to light absorption. To what extent light is scattered or absorbed by the particles, largely depends on their size, geometry and composition.^{16,36} For this reason, different heating capabilities can be expected depending on the structural characteristics of the octopods. How these parameters influence heat generation in bimetallic structures, including Pd content and its distribution, is an open question, though.

Thermal stability and heating efficiency

As previously mentioned, Au/Pd particles present a high thermal stability, though the threshold temperature at which reshaping becomes evident depends on the environment.²² In this work, octopods were dispersed in aqueous solution and thus temperature was limited by water evaporation. To test



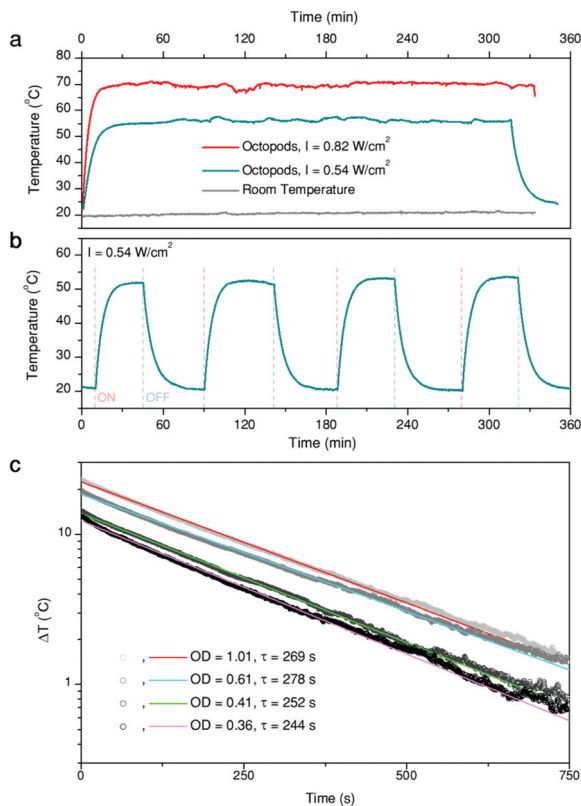


Fig. 3 Plasmonic heating: (a) Stability over time of the temperature generated by a 1 mL solution of octopods (Sample B) illuminated at two different light intensities, as indicated; (b) consecutive heating/cooling cycles by switching on and off the illumination source (c) cooling curves of four solutions with different concentrations of the same sample (OD at 808 nm are given in the legend). ΔT is the thermal increment, T_0 being room temperature. The lines represent single exponential fits, from which a time constant, τ , is obtained.

their thermal stability under these conditions, we monitored the temperature of a dispersion of octopods (1 mL, optical density of 0.51 at the laser wavelength) evenly illuminated at its whole surface with a laser of 808 nm wavelength. Temperature was monitored from the upper surface of the solution using a thermal camera. Examples of the heating curves obtained are shown in Fig. 3a and b, where the illumination intensity was limited to avoid evaporation of the solvent (condensation on the cuvette walls was already observed at 80 °C) and changes of sample concentration during the experiments.

Fig. 3a presents representative heating curves of sample B solution, illuminated at two different laser intensities. First, the profile confirms generation of heat when illuminated at 808 nm. The medium temperature keeps rising within a time-frame of about 10 min until thermal equilibrium is reached, with heat dissipation to the environment compensating the thermal energy provided by the particles upon illumination. Consequently, the maximum temperature depends on both the laser intensity and the environment, which does not change during the experiments (grey trace). Illumination over

5 h was applied to test the stability of the particles and the constancy of heat generation. The maximum temperature remains stable over the whole illumination time, apart from slight fluctuations due to the automatic electrical recalibration of the thermal imaging camera every few minutes (in our case ≈ 20 min), during the continuous sensor reading. This consistency indicates that the particles are thermally stable under the given conditions. As a further proof, extinction spectra of the sample solutions were measured before and after the experiments, to verify that the LSPR remained unaltered (Fig. S3c†). Additionally, no structural changes are evident from SEM characterization of the samples after heating (Fig. S3a and b†). Because the optical and structural properties did not show any noticeable changes, we confirm that the particles display a high thermal stability. The reproducibility of the heating (and cooling) curves was also tested (Fig. 3b) over four consecutive cycles, in which heating was triggered or stopped by switching the laser on and off.

Having tested the stability of the particles under the selected heating conditions, we studied the extent of light-to-heat conversion for different particle morphologies and compositions. For this purpose, we used the heating efficiency as a reference parameter, which enabled a fair comparison. Heating efficiency is the percentage of light that is transformed into heat, the maximum total energy being the total amount of intercepted photons, *i.e.* combined scattering and absorption contributions. Thus, assuming no additional ways to release energy into the environment (*e.g.* luminescence or chemical reactions), the heating efficiency is directly related to the ratio between extinction (the total spectral losses) and absorption, *i.e.* the losses that are transformed into heat. Based on thermal equilibrium equations, Roper *et al.*²⁶ developed an expression for the heating efficiency η , which depends solely on thermal and optical parameters:

$$\eta = \frac{\Delta Q}{P(1 - 10^{-OD})} \quad (1)$$

where P is the illumination power, OD the optical density of the sample at the illumination wavelength and ΔQ is the heat power released by the nanoparticles after subtracting any possible contributions from the solvent. ΔQ can be experimentally determined from the sample's thermal evolution over time after switching the illumination source on/off. In this work, it was deduced by fitting the cooling part of the thermal cycles to single exponential decays. As an example of the quality of the fit, four cooling curves measured for sample E are shown in Fig. 3c. ΔQ is deduced from the time constant, τ , of the exponential fit (for further details and plots of all the samples, see ESI, Fig. S5†).

The measured heating efficiency values are given in Table 1, together with the standard deviations, obtained from measuring several samples, as shown in Fig. 3c. The prepared particles feature heating efficiencies between 38% and 60%, showing that variability exists, as a function of composition and/or structure. To place these values in the context of cur-



rently existing optical heaters, we can compare them with the heating capacities of the best photothermal nanoparticles reported so far, which lie between 40% and 100%. Gold nanostars, for instance, typically exhibit efficiencies between 40% and 100% at 808 nm, depending on the morphology of their branches and tips;³⁷ gold nanorods can exhibit efficiencies between 50% and 95% at their longitudinal LSPRs, depending on their aspect ratio;^{37,38} and gold nanospheres can vary between 65% and 80% at 532 nm, depending on their diameter.³⁹ Accordingly, the heating efficiency of the octopods investigated here are within the range of the best photothermal probes proposed, though in the lower range, which appears to be a good starting point for bimetallic nanoparticles, especially given their increased thermal stability compared to gold-only structures. These results further indicate that for most optical applications, the photothermal ability of the nanoparticles should be considered as it may interfere with their performance as sensors or photocatalysts.

Just as observed for all these groups of gold nanoparticles, heat generation from bimetallic nanocrystals should be affected by several aspects related to their geometry and composition. Aiming to shed light on the parameters having a larger effect on heating efficiency, we plotted all the obtained results in a 3D correlation plot (Fig. 4a), and seeking for further details, heating efficiency was also plotted *vs.* tip-width (Fig. 4b), tip-base (Fig. 4c) tip-to-tip length (Fig. 4d), nanoparticle volume (Fig. 4e) and Pd content (Fig. 4f).

The high heating efficiency of gold nanostars was attributed to the presence of several thin and sharp tips.^{13,16} Based on this observation, tip-width seems to be a logical starting point. Fig. 4b shows two groups of particles: one with sharper tips of $Y \approx 10$ nm, and another with blunt tips of $Y \approx 27$ nm, *i.e.*, almost three times larger tip diameters. According to the obtained results, both groups contain particles with low heating efficiencies (38% and 39%, samples A and C, respectively), as well as particles with high heating efficiencies (60% and 48%, samples B and E, respectively). Considering the variability obtained within both groups, it can be hardly said that tip-width is strongly affecting heating efficiency. Of course, this does not mean that its effect is negligible, but it does not appear as the dominant aspect at this point.

Another parameter related to tip morphology is the tip base, Q , *i.e.* the branch base width. Its variability within the samples is smaller, but they could still be roughly grouped in two sets: $Q \approx 53$ nm and $Q \approx 64$ nm. Plotting heating efficiency *vs.* tip-base (Fig. 4c) suggests that smaller Q , *i.e.* thinner and slender branches (samples B, D, E) tend to account for higher heating efficiencies. This observation seems reasonable as heating is typically favoured by geometries in which most material is close to the surface, as the bulk contributes less.¹⁶ Also, the base width correlation shows high similarity to the tip-to-tip length, X , at least within the prepared particles. This suggests that the particles fall into the same groups, with the smaller particles ($X \approx 130$ nm) offering higher heating efficiencies above 40%, while the larger ones ($X \approx 144$ nm) fall below 40% (Fig. 4d). This relationship is con-

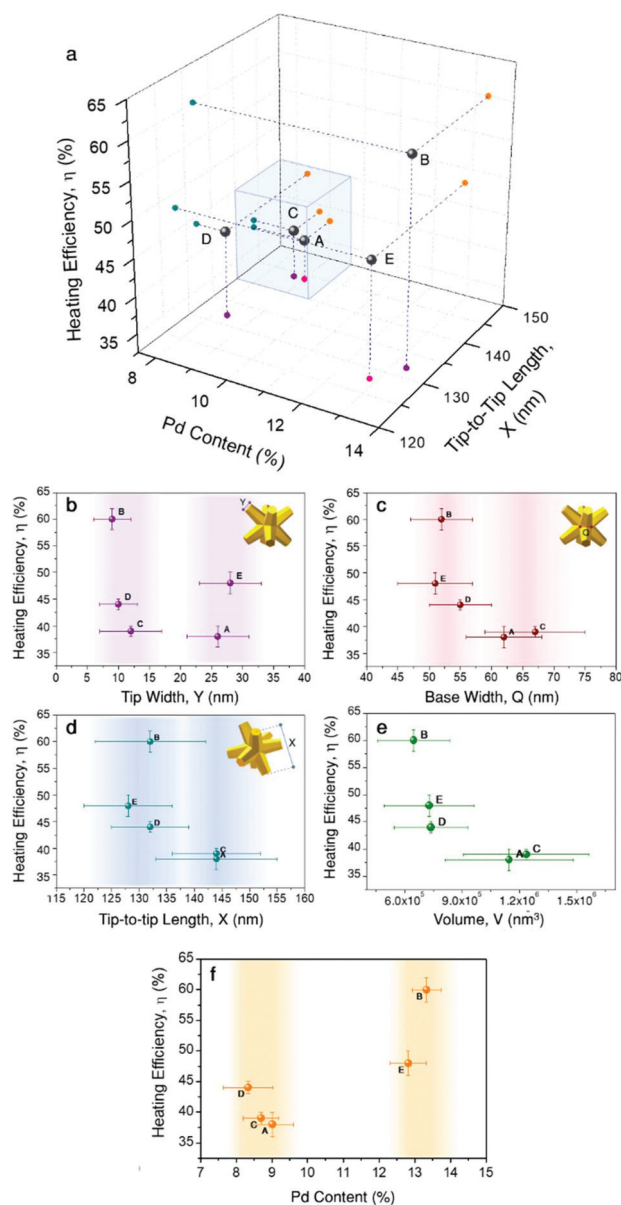


Fig. 4 Correlation of morphology and composition to heating efficiency: (a) 3D correlation plot of Pd content, X, and Y, which is shown in the lower plane with two different colours (pink ≈ 27 nm, purple ≈ 10 nm); the points encased in the blue cube correspond to a group of samples with larger X and higher Pd content. In the following graphs (b–f), heating efficiency is plotted individually *versus* the different parameters: (b) tip width, (c) branch base width, (d) tip-to-tip length, (e) nanoparticle volume, and (f) Pd content.

sistent within the indicated groups of particles, even though the tip-to-tip difference between both groups varies only by about 10%. Moreover, this agrees well with the general expectation that particles of larger sizes scatter more intensely, and thus their heating efficiency ought to be lower. Such a dependence becomes clearer if the heating efficiency is plotted *versus* the nanoparticle volume, V , which depends on every geometrical variable considered, X , Q , and Y , as given by eqn (S3).⁴⁰ Hence, it provides a more complete description. The obtained



ducing a volume of pure Au in the centre of the particle, the effective Pd content in the branched exterior is slightly increased (by approx. 10% for the given particle dimensions). Consequently, slightly lower Pd content is necessary to yield the same optical properties as in the first case (Fig. 5e). Apart from that, the gold core has no further influence on the optical properties which seems reasonable as localized surface plasmon resonances are essentially dictated by dielectric/metal interfaces, *i.e.* the external particle boundaries. For this reason, we consider in the next case that palladium is only present at the octopod tips, with the remaining particle consisting of gold (Fig. 5c). In direct comparison to the other models, the plasmon damping and broadening is more pronounced at similar Pd contents (Fig. 5f). Although the modes are broader, the absorption cross-sections are of similar intensity at the resonance position and the scattering losses are further reduced. Moreover, a 9% Pd content is already sufficient to balance absorption and scattering, whereas 18–20% Pd was required for the alloy models. This higher sensitivity of the optical properties for Pd located at the tips can be seen in the different changes of the absorption-to-extinction ratio (Abs/Ext) for variation of the Pd content (Fig. 5g). Here, the Abs/Ext ratio serves as a suitable quality factor, since absorption is associated with heating gain and extinction serves as a normalization parameter that also accounts for scattering losses in the light-to-heat conversion process. Accordingly, the maximum value Abs/Ext may take is 1, when no scattering losses are present. For the real system, the Pd distribution is complex. It should be noted that, electron tomography and EDS studies have revealed that the branches of the octopods are a gradient alloy, with significant accumulation of Pd at the tips.^{7,30}

Correlation between optical properties and heating efficiency

According to the above theoretical predictions, samples with higher Pd content present lower extinction cross-sections. Because this damping affects scattering more than absorption, heating efficiency improves. To verify this assumption, we performed diffuse reflectance (DR) spectroscopy using an integrating sphere. While standard transmission spectroscopy only quantifies the total extinction of light, DR measurements distinguish between absorption and scattering-related contributions. A specific set of experiments was thus performed with the sample being placed in an integrating sphere (see ESI, section ESI.2†).⁴³ This way, additional diffuse losses by scattering could be detected and evaluated. As a result, we obtained the transmittance of the octopod samples indicating significant differences in their spectral properties (Fig. 6a). While their extinction signatures, the sum of absorption and scattering, are in line with the results obtained from transmission vis/NIR spectroscopy (Fig. 2), the ratio of their diffuse contribution allows us to assess their suitability for heating by 808 nm illumination (Fig. 6b). Sample B shows not only the most favourable Abs/Ext ratio but also the most pronounced heating efficiency at 808 nm. Following this trend, the decrease in heating capacity of samples E, D, and A is nicely correlated

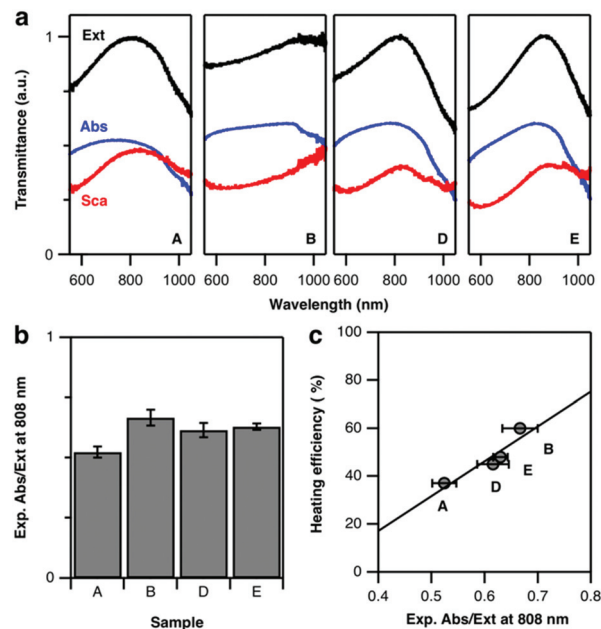


Fig. 6 Diffuse reflectance measurements: (a) representative transmittance spectra showing scattering (red), absorption (blue), and total extinction (black) of four samples: A and D with lower Pd content than B and E with higher Pd content; (b) experimental absorption/scattering ratio at 808 nm and (c) correlation to heating efficiency.

to their diffuse optical properties (Fig. 6c). Correlation between Abs/Ext and heating efficiency is expected, as the absorbed photons provide the energy available to heat up the sample. To have a complete picture, when connecting absorbance and heating, we should not forget about additional routes of energy dissipation. In particular, absorbed energy can also be released in a non-thermal way, starting with formation of hot electrons that may provide energy to chemical reactions on the surface, contributing to catalysis. This relaxation route typically presents a low probability, although the bimetallic character of the octopods can eventually play an important role on this aspect.^{44,45} Still, the thermal pathway is the main relaxation route, and thus diffuse reflectance indirectly allows for a comparison of the heating abilities of the nanoparticles.

It is worth discussing some additional important aspects that Fig. 6a (as well as the simulations in Fig. 5d–f) reveals: absorption and scattering curves show a spectral mismatch, *i.e.* their maxima are not at the same wavelength. Then, when both contributions are added to form the extinction spectrum, a single maximum is obtained, which we are considering as the main LSPR. This maximum, though, separates a range of lower wavelengths where absorption dominates, from a range of higher wavelengths with dominant scattering. In the context of heat generation, this indicates that illuminating at wavelengths below the LSPR maximum is favourable for heating. Going back to Fig. 2, this would mean that the excitation wavelength selection favours sample B over the others, which explains the large difference observed in heating efficiency. To test the impact of such a LSPR-excitation mismatch, we used



FDTD simulations to calculate the Abs/Ext ratio at 808 nm for octopods of different morphologies, varying X , Y , and Q (see Fig. S8†). Varying these geometrical parameters implies that the LSPR appears at different wavelengths, so this simulation considers both, resonant and off-resonance illuminations. When the LSPR is close to 808 nm, the theoretical predictions fully support the experimental hypothesis enunciated above that a smaller tip-to-tip distance, X , branch base width, Q , as well as smaller tip width, Y , are favourable for light-to-heat conversion. However, it seems also clear that when heating is required, those morphological properties should be combined with slightly blue-shifted illumination to match the absorption maximum.

Conclusions

Bimetallic gold–palladium nanoparticles with octopod shape were shown to display efficient photothermal effects and high thermal stability. Based on octopods with LSPRs close to 808 nm, we determined heating efficiencies between 40% and 60%. The highest efficiencies were observed for smaller octopods, with sharper tips, slender branches, and higher Pd content. By shifting any of these features, the efficiency was found to decrease by at least 10%. This shows how heating efficiency can be tuned to different needs. Indeed, for some geometries/compositions the local temperature released by the particles to their surroundings should be taken into account to understand their behaviour as sensors, as it may interfere with their sensing ability. Regarding catalysis, thermal modifications can be optically triggered, thus affecting reaction rates.

Our results demonstrate that the presence of Pd increases the absorption/extinction ratio. The distribution of Pd within the nanoparticles has a stronger effect when it is located at the tips, rather than inside the branches or the core. Consequently, the ratio between absorption and extinction, and the related suitability for different applications strongly depends on the amount and location of Pd. Finally, since absorption and scattering spectra present maxima at different wavelengths, heating was found to be favoured when the particles are illuminated at a wavelength slightly blue-shifted to the extinction maximum.

Conflicts of interest

There are no conflicts to declare.

Acknowledgements

S. E. S. and J. D. S. acknowledge support from the U.S. National Science Foundation award number CHE-1602476 and CHE-1904499. S. E. S. and her stay at CIC biomaGUNE was supported by a fellowship from the Fulbright U.S. Scholar Program. L. M. L.-M. acknowledges financial support from the Spanish Ministerio de Economía, Industria y Competitividad

(Grant MAT2017-86659-R) and the European Research Council (ERC AdG No. 787510, 4DbioSERS). C. K. acknowledges financial support from the European Commission under the Marie Skłodowska-Curie program (H2020-MSCA-799393, NANOBIOME). This work was performed under the María de Maeztu Units of Excellence Program from the Spanish State Research Agency – Grant No. MDM-2017-0720.

References

- 1 L. A. Kibler, A. M. El-Aziz, R. Hoyer and D. M. Kolb, *Angew. Chem., Int. Ed.*, 2005, **44**, 2080.
- 2 K. Deplanche, M. L. Merroun, M. Casadesus, D. T. Tran, I. P. Mikheenko, J. A. Bennett, J. Zhu, I. P. Jones, G. A. Attard, J. Wood, S. Selenska-Pobell and L. E. Macaskie, *J. R. Soc., Interface*, 2012, **9**, 1705.
- 3 D. Chen, J. Li, P. Cui, H. Liu and J. Yang, *J. Mater. Chem. A*, 2016, **4**, 3813.
- 4 P. Venkatesan and J. Santhanalakshmi, *Nanosci. Nanotechnol.*, 2011, **1**, 43.
- 5 G. J. Hutchings and C. J. Kiely, *Acc. Chem. Res.*, 2013, **46**, 1759.
- 6 H. Lin, Y. Chen and J. Shi, *Chem. Soc. Rev.*, 2018, **47**, 1938.
- 7 E. Ringe, C. J. DeSantis, S. M. Collins, M. Duchamp, R. E. Dunin-Borkowski, S. E. Skrabalak and P. A. Midgley, *Sci. Rep.*, 2015, **5**, 17431.
- 8 C. J. DeSantis and S. E. Skrabalak, *Langmuir*, 2012, **28**, 9055.
- 9 A. F. Smith, R. G. Weiner and S. E. Skrabalak, *J. Phys. Chem. C*, 2016, **120**, 20563.
- 10 S. Fischer, F. Hallermann, T. Eichelkraut, G. von Plessen, K. W. Krämer, D. Biner, H. Steinkemper, M. Hermle and J. C. Goldschmidt, *Opt. Express*, 2012, **20**, 271.
- 11 *Surface Enhanced Raman Spectroscopy: Analytical, Biophysical and Life Science Applications*, ed. S. Schlücker, Wiley-VCH, Weinheim, Germany, 2010.
- 12 G. Baffou, R. Quidant and F. J. García de Abajo, *ACS Nano*, 2010, **4**, 709.
- 13 G. Baffou and R. Quidant, *Laser Photonics Rev.*, 2013, **7**, 171.
- 14 M. B. Cortie, X. Xu, H. Chowdhury, H. Zareie and G. Smith, in *Smart Structures, Devices, and Systems II*, ed. S. F. Al-Sarawi, SPIE, Sydney (Australia), 2005, vol. 5649, p. 565.
- 15 C. J. DeSantis, A. C. Sue, M. M. Bower and S. E. Skrabalak, *ACS Nano*, 2012, **6**, 2617.
- 16 G. Baffou, R. Quidant and C. Girard, *Appl. Phys. Lett.*, 2009, **94**, 153109.
- 17 D. Jimenez de Aberasturi, A. B. Serrano-Montes, J. Langer, M. Henriksen-Lacey, W. J. Parak and L. M. Liz-Marzán, *Chem. Mater.*, 2016, **28**, 6779.
- 18 T. Vo-Dinh, Y. Liu, B. M. Crawford, H.-N. Wang, H. Yuan, J. K. Register and C. G. Khoury, *J. Immunol. Sci.*, 2018, **2**, 1.
- 19 H. Vanrompay, E. Bladt, W. Albrecht, A. Béché, M. Zakhosheva, A. Sánchez-Iglesias, L. M. Liz-Marzán and S. Bals, *Nanoscale*, 2018, **10**, 22792.



- 20 L. Rodríguez-Lorenzo, J. M. Romo-Herrera, J. Pérez-Juste, R. A. Alvarez-Puebla and L. M. Liz-Marzán, *J. Mater. Chem.*, 2011, **21**, 11544.
- 21 A. B. Taylor, A. M. Siddiquee and J. W. M. Chon, *ACS Nano*, 2014, **8**, 12071.
- 22 W. Albrecht, E. Bladt, H. Vanrompay, J. D. Smith, S. E. Skrabalak and S. Bals, *ACS Nano*, 2019, **13**, 6522.
- 23 F. Wang, C. Li, H. Chen, R. Jiang, L.-D. Sun, Q. Li, J. Wang, J. C. Yu and C.-H. Yan, *J. Am. Chem. Soc.*, 2013, **135**, 5588.
- 24 C.-C. Chang, H.-L. Wu, C.-H. Kuo and M. H. Huang, *Chem. Mater.*, 2008, **20**, 7570.
- 25 R. G. Weiner, C. J. DeSantis, M. B. T. Cardoso and S. E. Skrabalak, *ACS Nano*, 2014, **8**, 8625.
- 26 D. K. Roper, W. Ahn and M. Hoepfner, *J. Phys. Chem. C*, 2007, **111**, 3636.
- 27 *Handbook of Optical Constants of Solids*, ed. E. D. Palik, Academic Press, San Diego (CA), USA, 1991.
- 28 P. Johnson and R. Christy, *Phys. Rev. B: Solid State*, 1972, **6**, 4370.
- 29 C. J. DeSantis, A. A. Peverly, D. G. Peters and S. E. Skrabalak, *Nano Lett.*, 2011, **11**, 2164.
- 30 A. F. Smith, R. G. Weiner, M. M. Bower, B. Dragnea and S. E. Skrabalak, *J. Phys. Chem. C*, 2015, **119**, 22114.
- 31 A. M. Smith, M. C. Mancini and S. Nie, *Nat. Nanotechnol.*, 2009, **4**, 710.
- 32 E. Hemmer, P. Acosta-Mora, J. Mendez-Ramos and S. Fischer, *J. Mater. Chem. B*, 2017, **5**, 4365.
- 33 M. A. Miller, B. Askevold, H. Mikula, R. H. Kohler, D. Pirovich and R. Weissleder, *Nat. Commun.*, 2017, **8**, 15906.
- 34 R. M. Yusop, A. Unciti-Broceta, E. M. V. Johansson, R. M. Sánchez-Martín and M. Bradley, *Nat. Chem.*, 2011, **3**, 239.
- 35 N. Neubauer, J. Palomaeki, P. Karisola, H. Alenius and G. Kasper, *Nanotoxicology*, 2015, **9**, 1059.
- 36 J. Stehr, C. Hrelescu, R. A. Sperling, G. Raschke, M. Wunderlich, A. Nichtl, D. Heindl, K. Kürzinger, W. J. Parak, T. A. Klar and J. Feldmann, *Nano Lett.*, 2008, **8**, 619.
- 37 L. M. Maestro, P. Haro-Gonzalez, A. Sanchez-Iglesias, L. M. Liz-Marzan, J. García Solé and D. Jaque, *Langmuir*, 2014, **30**, 1650.
- 38 J. R. Cole, N. A. Mirin, M. W. Knight, G. P. Goodrich and N. J. Halas, *J. Phys. Chem. C*, 2009, **113**, 12090.
- 39 K. Jiang, D. A. Smith and A. Pinchuk, *J. Phys. Chem. C*, 2013, **117**, 27073.
- 40 C. J. DeSantis, A. C. Sue, A. Radmilovic, H. Liu, Y. B. Losovyj and S. E. Skrabalak, *Nano Lett.*, 2014, **14**, 4145.
- 41 S. Y. Lee and J. W. Ha, *Phys. Chem. Chem. Phys.*, 2016, **18**, 32682.
- 42 U. Aslam, S. Chavez and S. Linic, *Nat. Nanotechnol.*, 2017, **12**, 1000.
- 43 R. P. M. Höller, M. Dulle, S. Thomä, M. Mayer, A. M. Steiner, S. Förster, A. Fery, C. Kuttner and M. Chanana, *ACS Nano*, 2016, **10**, 5740.
- 44 K. Sytwu, M. Vadai and J. A. Dionne, *Adv. Phys.: X*, 2019, **4**, 1619480.
- 45 S. Chavez, U. Aslam and S. Linic, *ACS Energy Lett.*, 2018, **3**, 1590.

